www.nature.com/aps

Acta Pharmacologica Sinica

ARTICLE

Involvement of cell shape and lipid metabolism in glioblastoma resistance to temozolomide

Munki Choo[1], Van-Hieu Mai[1], Han Sun Kim[1], Dong-Hwa Kim[1], Ja-Lok Ku[2], Sang Kook Lee[1], Chul-Kee Park[3], Yong Jin An[1] and Sunghyouk Park[1]

Temozolomide (TMZ) has been used as standard-of-care for glioblastoma multiforme (GBM), but the resistance to TMZ develops quickly and frequently. Thus, more studies are needed to elucidate the resistance mechanisms. In the current study, we investigated the relationship among the three important phenotypes, namely TMZ-resistance, cell shape and lipid metabolism, in GBM cells. We first observed the distinct difference in cell shapes between TMZ-sensitive (U87) and resistant (U87R) GBM cells. We then conducted NMR-based lipid metabolomics, which revealed a significant increase in cholesterol and fatty acid synthesis as well as lower lipid unsaturation in U87R cells. Consistent with the lipid changes, U87R cells exhibited significantly lower membrane fluidity. The transcriptomic analysis demonstrated that lipid synthesis pathways through SREBP were upregulated in U87R cells, which was confirmed at the protein level. Fatostatin, an SREBP inhibitor, and other lipid pathway inhibitors (C75, TOFA) exhibited similar or more potent inhibition on U87R cells compared to sensitive U87 cells. The lower lipid unsaturation ratio, membrane fluidity and higher fatostatin sensitivity were all recapitulated in patient-derived TMZ-resistant primary cells. The observed ternary relationship among cell shape, lipid composition, and TMZ-resistance may be applicable to other drug-resistance cases. SREBP and fatostatin are suggested as a promising target-therapeutic agent pair for drug-resistant glioblastoma.

Keywords: glioblastoma; temozolomide resistance; cell shape; lipid metabolism; SREBP; fatostatin

Acta Pharmacologica Sinica (2023) 44:670–679; https://doi.org/10.1038/s41401-022-00984-6

INTRODUCTION

Glioblastoma multiforme (GBM) is one of the deadliest cancers, with the median overall survival of about 6 months without treatments and about 15 months with treatments [1–5]. The treatment options are quite limited and include surgical excision, radiation, and adjuvant chemotherapy [6]. The only oral anticancer drug currently available is a cytotoxic agent temozolomide (TMZ) that acts through DNA methylation leading to mismatched base pairing [7]. However, the resistance to TMZ develops quickly and frequently [8–10]. The main mechanism of TMZ resistance has been suggested to involve methyl guanosine methyltransferase (MGMT) overexpression that removes the methyl group from the modified DNA bases [11]. The MGMT expression is regulated by the promoter methylation which is used as a surrogate marker for TMZ resistance. Recent research, however, suggested that there can be other mechanisms for TMZ resistance, including ROS generation, autophagy, epigenetic modifications, microRNAs, and extracellular vesicle production [12, 13]. Therefore, the mechanism of TMZ resistance may vary across individual cases of GBM, and further studies are warranted to fully understand and to apply it to better therapeutic approaches.

Lipids are important cellular components involved in a variety of biological functions such as energy storage, cell signaling, and even cell shape [14, 15]. For brain cancers, lipid profiles were found different from those of normal brain tissues or other cancers. For example, the amount of lipids in tumor tissues was greater than in normal tissues in malignant gliomas [16], and more free fatty acids (FA) were found in several brain tumor than in normal brain tissue [17]. In addition, triglycerides (TG) were found in untreated GBM, but not in healthy adult brain tissues [18], and the levels of phosphatidylcholine were significantly higher in medulloblastoma and GBM than in normal brain tissues [16, 18]. Not only the amount, but also the chemical nature of lipids varied. Cholesterol esters (CE) formed by esterification of cholesterol and long-chain FA were found only in high-grade gliomas [18]. Interestingly, FA saturation also varied, with polyunsaturated FA, particularly linoleic acids, being more abundant in brain tumors than in normal brain tissues. In addition, the unsaturation of FA in normal brain was ~35%, compared to 68% in gliomas, ~46% in neurinomas, and ~61% in carcinomas [17].

Resistance to chemotherapy occurs by multi-factorial causes, and changes in lipids were implicated in drug resistance in several cancers. When breast cancer cells developed doxorubicin resistance, increased cholesterol level caused lower membrane permeability leading to drug resistance [19]. In addition, cholesterol content was directly proportional to the drug resistance, and drug-sensitivity caused by cholesterol deficiency was reversed by cholesterol reload in vincristine-resistant murine leukemia [20]. The cancer drug resistance was also found to be associated with physical properties such as cell shapes. These

[1]Natural Product Research Institute, College of Pharmacy, Seoul National University, Seoul 08826, Korea; [2]Korean Cell Line Bank, Laboratory of Cell Biology, Cancer Research Institute, College of Medicine, Seoul National University, Seoul 03080, Korea and [3]Department of Neurosurgery, College of Medicine, Seoul National University, Seoul 03080, Korea
Correspondence: Yong Jin An (biochem.yong@gmail.com) or Sunghyouk Park (psh@snu.ac.kr)

Received: 14 April 2022 Accepted: 12 August 2022
Published online: 13 September 2022

were demonstrated for cisplatin-resistance in endometrial cancer cells [21] and doxorubicin-resistance in estrogen receptor positive [22] or triple-negative breast cancer cells [23]. Interestingly, the cell shape changes were also connected to lipids that are components of cell membrane. Breast cancer cells changed shapes with concomitant increase in lipid droplets upon hormone treatment [24], and cell shape and lipid composition changes were also observed in erythroid cells exposed to toxic environment [25]. Collectively, these results show that there are binary relationships among these important phenotypes: lipid-drug resistance, drug-resistance-shape, and shape-lipid. Tantalizingly, the ternary relationship among shape-lipid-drug resistance has not been explored in one system, particularly in GBM. Therefore, we employed NMR-lipidomics and molecular biological tools to investigate how the three important phenotypes are linked in TMZ resistance for GBM cells. We also sought to find a therapeutic approach to overcome the resistance by targeting lipid metabolism.

MATERIALS AND METHODS

Sample preparation for NMR metabolomics and NMR measurement

The metabolites were extracted using the two-phase methanol-chloroform extraction method. Methanol (600 µl) was sprayed on the cell plate, and cells were transferred to a 2 ml microtube by scraping, after which 300 µl of chloroform was added. Three cycles of the following steps were then repeated: vigorous vortexing for 30 s, dipping into liquid nitrogen for 1 min, and thawing at room temperature for 2 min. After the addition of a mixture of 300 µl chloroform and 300 µl distilled water, the samples were centrifuged at 15,800 × *g* for 20 min at 4 °C. The upper water phase and lower lipid phase were collected and dried with a centrifugal vacuum evaporator (Vision, Seoul, Korea). The lower phase pellets were dissolved in 500 µl $CDCl_3$ (Sigma-Aldrich, MO, USA) for NMR analysis. NMR spectra were measured on an 800 MHz Bruker Ascend spectrometer (Bruker, MA, USA) equipped with a cryogenic triple resonance probe. Two-dimensional NMR spectra were obtained with a typical ^{1}H–^{13}C Heteronuclear Single Quantum Coherence (HSQC) pulse sequence, as described previously [26]. The acquisition and processing of the raw data were performed using the vendor-provided software. The peaks were referenced to the peak of chloroform ($^{1}H = 7.25$ ppm, $^{13}C = 38.2$ ppm).

Patient-derived primary cells

The patient-derived immortalized primary cells were obtained from Korean Cell Line Bank (Seoul, Korea). Cells with MGMT promoter methylated were considered TMZ-sensitive (SNU-3987, SNU-4702, and SNU-5262). Cells with MGMT promoter unmethylated were considered TMZ-resistant (SNU-4026, SNU-4072, and SNU-4177). The actual TMZ-resistance status was experimentally determined by measuring the IC_{50} values toward TMZ. All of these cells had isocitrate dehydrogenase wild type status.

Chemicals and reagents

The inhibitor for SREBP, fatostatin (MER-341329-25M) was purchased from Merck (Darmstadt, Germany). Temozolomide (TMZ) (T2744) was purchased from TCI Chemical (Tokyo, Japan). All reagents not mentioned were purchased from Sigma (St. Louis, MO, USA). Antibodies for β-actin (sc-47778, 1:1000), SREBP2 (sc-13552, 1:500) were from Santa Cruz Biotechnology (Santa Cruz, CA, USA), and the second antibody for mouse (GTX213111-01, 1:10,000) was from GeneTex (GeneTex, CA, USA).

Cell culture and stable isotope labeling

TMZ-resistance U87 (U87R) cells were established as described before [27] and maintained in RPMI-1640 (Welgene, Gyeongsan-si, Korea). All culture media were supplemented with 10% fetal bovine serum (FBS, Welgene, Gyeongsan-si, Korea), 1% penicillin/streptomycin (Gibco, NY, USA) and incubated at 37 °C under 5% of CO_2 humidified air. For stable isotope labeling, 11 mM of [U-^{13}C] glucose (CLM-1396-5, Cambridge Isotope Laboratories, MA, USA) was added to glucose-free RPMI (11879020, Gibco, NY, USA) with 10% dialyzed FBS (26400044, Gibco, NY, USA) and the cells were incubated for overnight at 37 °C.

Western blot

Western blot was performed following as standard protocol. The primary antibody was incubated with the blot membrane at 4 °C overnight and followed by incubation with secondary antibody in 2.5% skim milk TBST at room temperature for 1 h. The protein bands were visualized using the enhanced chemiluminescence detection kit (GE Healthcare Life Science, Little Chalfont, UK). Blots were analyzed by LAS4000 (GE Healthcare, ImageQuant).

Oil Red O staining for lipid droplet

In 10 ml of 100% Propylene Glycol (PEG, P355-1, Fisher Scientific, Cleveland, OH, USA), 0.5 g of oil red O (ORO) dye was dissolved. While heating the solution to 95 °C, additional 90 ml of PEG was gradually added. The solution was then filtered with Whatman No. 4 filter paper (GE Healthcare, Buckinghamshire, UK). ORO dye solution (in PEG) were filtered with filter paper. The cells were fixed with 4% paraformaldehyde and then stained with ORO solution. After staining, stained cells were photographed under the microscope (Olympus, IX70). The white balance was adjusted, and then the images were analyzed by ImageJ.

BODIPY staining for lipid droplet

U87 cells and U87R cells (8×10^5 cells/well) were seeded in a confocal dish (SPL Life Sciences, Gyeonggi-do, Korea) coated with 0.2% gelatin and incubated overnight at 37 °C under 5% of CO_2 humidified air. Cells were treated with media (RPMI) containing 50 µM of BODIPY® FL C12 (MOP-D-3822, Millipore Sigma), followed by incubation under 5% of CO_2 for 30 min in a shaded state. After washing with DPBS, normal RPMI growth media was added. Images were taken using a Confocal Laser Scanning Microscope (SP8 X, Leica) at Seoul National University National Instrumentation Center for Environmental Management. PMT mode, ×100 objective and 80% argon power at 37 °C, under 5% CO_2/95% air environmental condition was used.

Cell proliferation assay with CCK-8

The viability of glioma cells from each group was measured using a D-Plus™ CCK cell viability assay kit (Dongin biotech, Seoul, Korea) according to the manufacturer's instructions. Briefly, U87 cells (2×10^3 cells/well), U87R cells (1×10^3 cells/well), TMZ-sensitive primary cells (5×10^3 cells/well) and TMZ-resistant primary cells (2.5×10^3 cells/well) were seeded in 96-well plates, incubated for 24 h, and then treated for 5 days with the drugs. After treatment, 10 µl of CCK-8 solution was added to the 200 µl cell medium of each well and the cells were incubated for 4 h at 37 °C in the dark. The absorbance at 450 nm was measured with a microplate reader (Molecular Devices VersaMax, Sunnyvale, CA, USA), and IC_{50} values were calculated by nonlinear regression analysis using OriginPro 8 (OriginLab Corporation, Northampton, MA, USA).

RNA isolation and microarray analysis

Total RNA was isolated from cell lines by easy-spin™ total RNA extraction kit (Intron, Seoul, Korea) following the manufacturer's instruction. Each RNA sample was analyzed with SurePrint G3 Human Gene Expression Microarrays, 8 × 60K v2 (Agilent Technologies, Santa Clara, CA, USA). Following fragmentation, cRNA were hybridized to the Agilent expression microarray according to the protocols provided by the manufacturer. Arrays were scanned using the Agilent Technologies G4900DA SG12494263. Array data

export processing and analysis was performed using Agilent Feature Extraction v11.0.1.1. Microarray GEO accession number is GSE193957.

Cell membrane fluidity measurement

Cell membrane fluidity was measured with a membrane fluidity kit (#ab189819, Abcam, Cambridge, MA, USA) following the manufacturer's instruction. U87 cells (1×10^4 cells/well) and U87R cells (1×10^4 cells/well) were seeded in 96-well plates, incubated for overnight, and then treated with the labeling solution (100 µl) and incubated at 25 °C for 20 min under continuous shaking. By quantifying the ratio of excimer (450 nm) to monomer (400 nm) fluorescence (Molecular Devices, SpectraMAX M5), the membrane fluidity was calculated. The data were indicated as the ratio between pyrene excimer and monomer (ratio I_e/I_m).

Synergistic anticancer activity test

Serial concentrations of TMZ and fatostatin were used based on the IC_{50} values for each cancer cell line. The synergistic effect was determined with CompuSyn software version 1 [28]. The combination index (CI) of $CI < 1$, $CI = 1$, and $CI > 1$ indicated synergism, additiveness, and antagonism effects of the combination, respectively.

Transwell migration assay

Transwell chambers (24 wells plate, 8 µm pore size, SPL 37224) were used to test migration ability. Cells were suspended in serum-free RPMI and counted to a density of 1×10^6 cells/ml. The upper chamber of the migration well was seeded with 100 µl of cell suspension. RPMI with 10% FBS was loaded into the lower chamber for chemoattractant. Cells were incubated for 1 day at 37 °C. Using a cotton swab, cells from the top of the filter were removed. Cells that had passed through to the bottom of the insert membranes were fixed and stained with 0.5% crystal violet solution with 20% methanol for 20 min. After staining, stained cells were photographed under the microscope (Olympus CKX41, Tokyo, Japan) with the camera (MD800E, AmScope, Iscope Corp, Chino, CA, USA).

Gene knockdown using siRNA transfection and real-time PCR analysis

The predesigned siRNAs targeting *SREBF1*, *SREBF2*, and *FASN* were purchased from Bioneer (Daejeon, Korea). Negative control siRNA from the same company was used for control. The cells were transfected with 100 nM siRNA using Lipofectamine RNAiMAX for 48 h (Thermo Fisher Scientific, Waltham, MA, USA) according to the manufacturer's protocol. The media were changed with fresh media and colorimetric cell viability assays were conducted with D-Plus™ CCK cell viability assay kit (Dongin biotech, Seoul, Korea) after 24 h. The cellular viability was measured with absorbance at 450 nm by a microplate reader. Total RNA was isolated from cell lines by easy-spin™ total RNA extraction kit (Intron, Seoul, Korea). The cDNA was synthesized by High capacity cDNA reverse transcription kit (Applied Biosystem, Foster City, USA) following the manufacturer's instruction. Real-time PCR reaction was performed in triplicate in an Applied Biosystems 7300 PCR machine with SYBR green-based detection (iTaq ™ Universal SYBR Green Supermix, Bio-Rad, USA). The gene expression ΔCt values from PCR were calculated by normalization with *β-actin*. The primers of *SREBF1*, *SREBF2* and *FASN* were purchased from Bioneer. The primer sequences of *β-actin* are as follows: sense: 5′-GGACTTCGAGCAAGAGATGG-3′, antisense: 5′-AGCACTGTGTTGGCGTACAG-3′.

Statistical analysis

The statistical analysis between two groups was performed using Prism (version 9.0.0, GraphPad Software). Depending on the *P* value of the *F*-test (cutoff of 0.05), the Student's *t*-test or Welch's *t*-test was used. Error bars in the graphs show the standard deviation.

RESULTS

Morphological difference between TMZ-sensitive and resistant glioblastoma cells

To study the cell shape-TMZ resistance relationship in glioblastoma, a TMZ-resistant cell line was established as described before [12, 27]. The sensitivity of the resistant cells (U87R) to TMZ was about 13 times lower than that of the sensitive cells (U87), as evaluated by the IC_{50} values (Fig. 1a, b). When observed under a microscope, U87 cells exhibited pointed, thin, and long morphology, similar to that of neurons (Fig. 1b). On the other hand, U87R cells were more rounded and had larger cytoplasmic part. The difference in shape upon acquired drug resistance was also observed in an unrelated drug-cancer combination. Lung cancer cells that are resistant to gefitinib exhibited more elongated shape than the parent cells that are sensitive to the drug (Supplementary Fig. S1). These suggest that drug resistance may be commonly accompanied by changes in the cell shape.

TMZ resistance linked to lipid composition and cell membrane fluidity

We hypothesized that this shape-resistance relationship may be related with lipid composition and metabolism, as lipid is the primary component of cell membrane that determines the cell shape. In addition, lipid in the cell membrane is the first barrier for drug's passage to cellular targets. To test this hypothesis, we employed NMR lipidomics and compared the lipid composition in

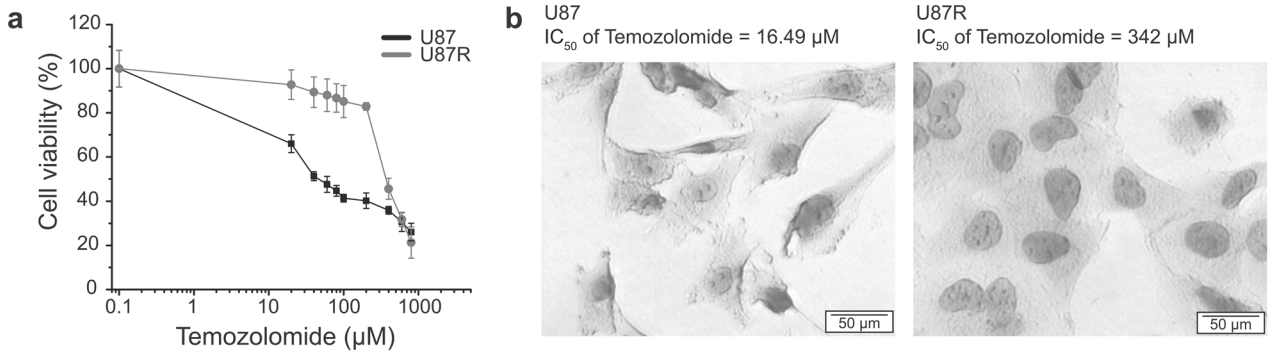

Fig. 1 The morphology of glioblastoma cell lines according to drug sensitivity. a Dose-response curves of U87 (black) and U87-temozolomide resistant (U87R, gray) cells after 5-day incubation with the temozolomide, as determined by CCK-based assay. Error bars represent standard deviations. **b** The morphology difference between drug sensitive and resistance cell line observed with light microscopy. Cells were stained with Hematoxylin. U87 cells (left) and U87R cells (right).

U87 and U87R. We obtained ^{1}H-^{13}C HSQC spectra of the extracts of both TMZ-sensitive and resistant cell extracts labeled with [U-^{13}C]glucose. The usage of the two-dimensional NMR and stable isotope labeling greatly enhanced the resolution and the sensitivity of the raw data, enabling confident quantitative analysis of the lipid species (Fig. 2a and Supplementary Table S1). The orthogonal projections to latent structures-discriminant analysis on the NMR spectra provided clean separation between U87 and U87R cells according to the lipid composition (Q^2 value of 0.996 and R^2Y value of 0.999; Fig. 2b). From the multivariate statistical analysis on the peak volume of 2D-HSQC data, lipid species contributing to the difference could be identified (Fig. 2c). In U87R, the levels of diglyceride, cholesterol (CH), and overall FA were higher whereas those for TG and CE were lower. The lower levels of TG and CE, the major forms of stored lipids in the lipid droplets [29], were also confirmed by ORO and BODIPY staining (Fig. 2d–f). This suggests that cholesterol and FA are synthesized more but not stored in lipid droplets and that those may be used to support membrane biogenesis in U87R cells. Interestingly, the levels of unsaturated FA were not different (Fig. 2c), but the FA unsaturation ratio decreased (Fig. 2g), most probably due to the increased overall FA in U87R. These results show that there is significant difference in lipid usage and composition between U87 and U87R cells. As these changes in lipids can affect cell membrane fluidity, we measured it with a pyrene-based fluorescence method. In U87R cells, the excimer/monomer ratio of the pyrene probe was low, indicating that the membrane fluidity is reduced (Fig. 2h). There were previous studies showing that membrane fluidity and migration were proportional [30–32]. When we compared U87 and U87R in transwell assay, U87 cells migrated more than U87R cells. (Supplementary Fig. S2). Therefore, the changes in lipid composition affecting membrane fluidity may also have an effect on cell's migratory phenotype. Taken together, the increase in cholesterol and the lower unsaturated FA ratio in U87R cells should contribute to the lower membrane fluidity of the U87R cells. This also indicates that there is a relationship among TMZ resistance, lipid composition, and membrane fluidity.

Lipid-related metabolic pathways in TMZ-sensitive and resistant glioblastoma cells

To explain these phenotypic compositional changes in lipids according to the TMZ resistance, we performed transcriptomic analysis on U87 and U87R cells with microarray. Gene set enrichment analysis with the reactome gene set revealed that "cholesterol biosynthesis" and "regulation of cholesterol biosynthesis by sterol regulatory element-binding protein (SREBP)" were among the top enhanced pathways in U87R cells (Fig. 3a). In the enrichment plot of the latter pathway, fatty acid synthase (*FASN*), acetyl-coenzyme A carboxylase alpha (*ACACA*), sterol regulatory element-binding transcription factor 2 (*SREBF2*), and 3-hydroxy-3-methyl-glutaryl-coenzyme A reductase (*HMGCR*) were also found in the leading edge for U87R. As *SREBF* is a master regulator for lipid synthesis, we compared the protein expression levels of its isoforms and downstream lipid synthesis-related proteins (e.g., SREBP1, SREBP2, ACC, FASN, 3-hydroxy-3-methyl-glutaryl-coenzyme A synthase (HMGCS), HMGCR, mevalonate diphosphate decarboxylase (MVD), and squalene monooxygenase (SQLE)). The results showed that the levels of important factors and enzymes for cholesterol and FA synthesis were generally higher in U87R cells. These included the mature form of SREBP2, enzymes for FA synthesis (FASN and ACC), and those for cholesterol synthesis (HMGCS and MVD) (Fig. 3b–d). Overall, our gene and protein expression analysis is consistent with the metabolomics results showing higher cholesterol and FA levels, supporting lower membrane fluidity in TMZ-resistant U87R cells, and suggest that lipid metabolism is linked to drug resistance in GBM cells.

Inhibitors of lipid synthesis enzymes can overcome drug resistance in U87R cells

To see if we can exploit the higher lipid synthetic activity of U87R cells in overcoming the TMZ resistance, we tested several inhibitors of the lipid synthesis proteins which are upregulated in U87R. We also tested the effects of knockdown of *SREBF1*, *2* and *FASN*. The knockdown of *SREBF1*, *2* and *FASN* resulted in a notable decrease in cell confluency and viability for the U87R cells. The effects were significantly larger in U87R cells than U87 cells, showing that U87R was more vulnerable to the knockdowns of lipid synthesis than U87 (Supplementary Fig. S3). Therefore, both pharmacological and genetic approaches consistently show that the TMZ resistance is associated with higher lipid synthesis. These included an SREBP inhibitor fatostatin, an ACC inhibitor TOFA, and a FASN inhibitor C75 that have not yet been tested in GBM. All these inhibitors exhibited several times lower or at least similar IC_{50} values for U87R cells than for U87 cells, which is remarkable considering that U87R cells are 21 times less sensitive to TMZ than U87 cells (Fig. 4a–c and Table 1). In addition, fatostatin was ~45 times more potent than TMZ for U87R cells, exhibiting the lowest IC_{50}. To further test the utility of fatostatin for TMZ-resistant cells, we investigated if fatostatin can give synergy with TMZ which has been used as the standard-of-care for decades. As shown in Fig. 4d, e, the addition of fatostatin (20 μM) greatly lowered the cell viability for U87R cells across all the TMZ concentrations (58%–7%), whereas the effect on U87 cells were smaller. The synergy between fatostatin and TMZ was assessed quantitatively in the full ranges of both drugs using the combination index (Supplementary Table S2) [28]. Fatostatin exhibited synergy with TMZ (combination index <1) for 7 out of 16 concentration combinations for U87R. Overall, these results suggest that SREBP-dependent lipid synthesis that can affect membrane composition and fluidity [33] is a new vulnerability of TMZ-resistant GBM cells and that fatostatin and lipid synthesis enzyme inhibitors may be used in place of or with TMZ to inhibit GBM cell growth.

Primary GBM cells with TMZ resistance exhibit different lipid composition and are sensitive to fatostatin

The above results were obtained with laboratory cell lines with acquired TMZ-resistance. For clinical relevance of our results, we further investigated if those results could be reproduced in patient-derived primary GBM cells. We obtained primary immortalized GBM cells, three with and the other three without MGMT promoter methylation. We confirmed that all three cells with the MGMT methylation had much higher IC_{50} to TMZ, exhibiting TMZ resistance status (Fig. 5a and Supplementary Table S3). TMZ-sensitive primary cells (SNU-3987, SNU-4702, and SNU-5262) were stretched and sharp. On the other hand, TMZ-resistant primary cells (SNU-4026, SNU-4072, and SNU-4177) were more spherical and flat, consistent with those for the U87 and U87R (Fig. 5b). In addition, these cells exhibited similar ORO staining pattern with U87 and U87R cell lines, according to their TMZ-resistance (Fig. 5c, d). Importantly, lipid analysis confirmed that the FA unsaturation ratio was lower in the TMZ-resistant cells as in U87R cells (Fig. 5e) due to the increase in FA level (Fig. 5f). Furthermore, the decrease in membrane fluidity in the TMZ-resistant cells was observed (Fig. 5g), suggesting that the membrane fluidity-drug resistance relationship in the U87R cells also holds for these primary cells. Then, we compared the efficacy of lipid-metabolism-related drugs for these patient-derived cells. Despite much lower TMZ sensitivity (~33 fold) for the resistant cells than sensitive cells, fatostatin effectively inhibited the resistant cells ($IC_{50} < 15$ μM for all the cells), which is comparable to the potency of TMZ to sensitive cells. TOFA and C75 also exhibited lower or similar IC_{50} values for the resistant cells compared to those for the sensitive cells (Table 2 and Supplementary Fig. S4). Taken together, the results for shape-lipid-resistance relationship obtained with the laboratory cell lines were recapitulated in the primary cells.

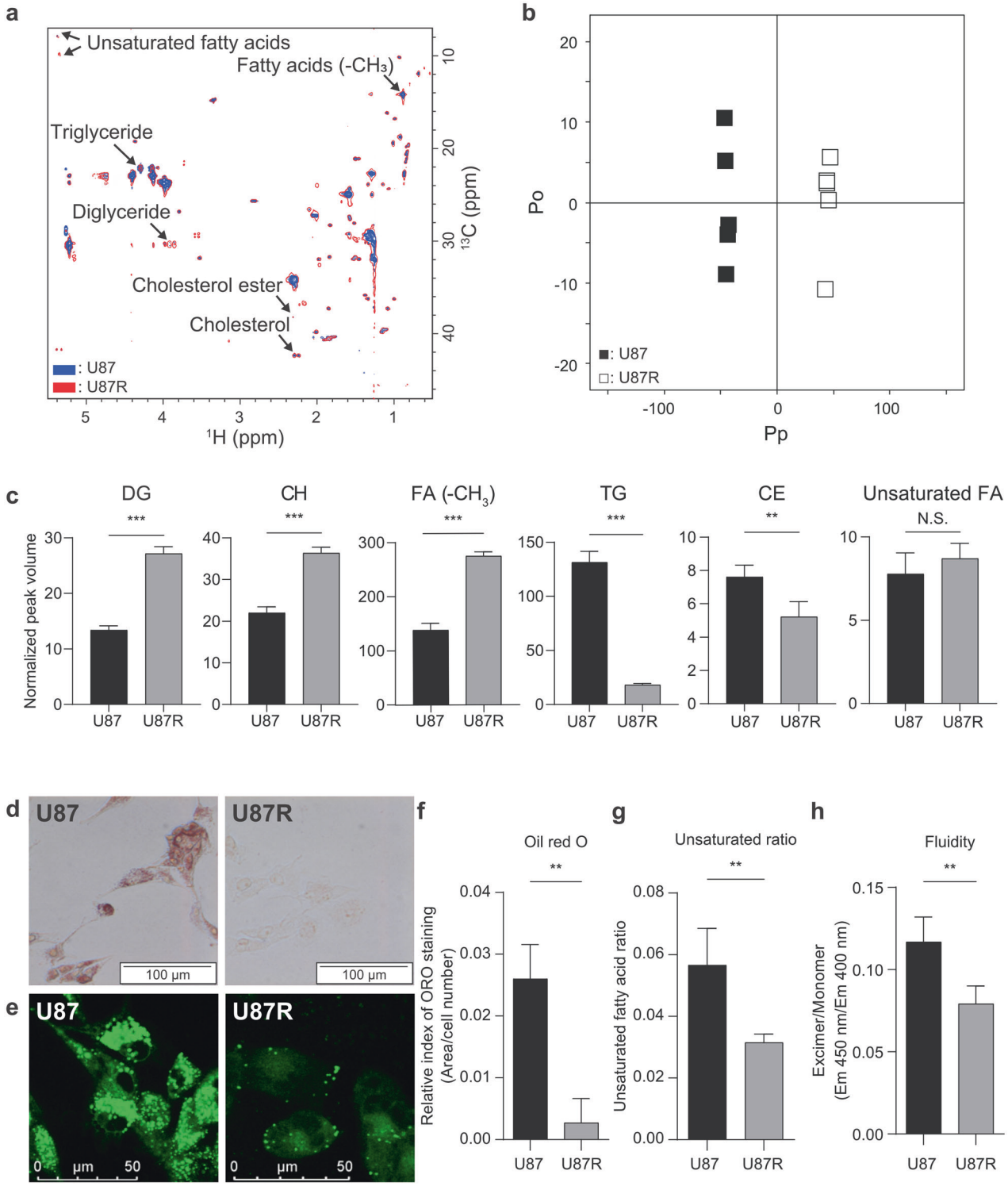

Fig. 2 NMR-based lipid metabolomics and lipid phenotypes of U87 and U87R cells. a HSQC spectra of lipid extracts from U87 and U87R cells after overnight labeling with [U-^{13}C]glucose. U87 (blue) and U87R (red) spectra are overlaid. Key lipid species are labeled (see Supplementary Table S1). **b** OPLS-DA score plot for the lipidomic results showing the discrimination between U87 and U87R cells. The model was obtained using one predictive and one orthogonal components. U87: filled boxes, U87R: open boxes. Pp represents the predictive component and Po represents the orthogonal component. **c** Levels of key lipid species in U87 and U87R cells. The levels were determined by the mean peak volumes normalized by the total volume from the HSQC spectra (**a**) ($n = 5$). ORO (**d**) and BODIPY (**e**) staining of glioblastoma cell lines. Images were acquired by light microscopy and fluorescence microscopy, respectively. **f** Quantitation of ORO staining in **d** with ImageJ software. The staining levels were normalized against cell numbers ($n = 3$). **g** Fatty acid unsaturation ratio. The values were obtained by dividing the peak volumes of unsaturated FA peak (^{1}H = 5.35 ppm, ^{13}C = 9.81 ppm) to those of total FA peak (^{1}H = 0.88 ppm, ^{13}C = 14.27 ppm) from the peak volumes of HSQC spectra (**a**). **h** Membrane fluidity of glioblastoma cell lines measured by the ratio of the fluorescence of pyrene excimer (E_x/E_m = 360/450 nm) to monomer (E_x/E_m = 360/400 nm) ($n = 6$). All statistical analysis was performed using the unpaired *t*-test, and the resulting *P* values are $^*P < 0.05$, $^{**}P < 0.01$, $^{***}P < 0.001$ and N.S. not significant. Error bars represent standard deviations.

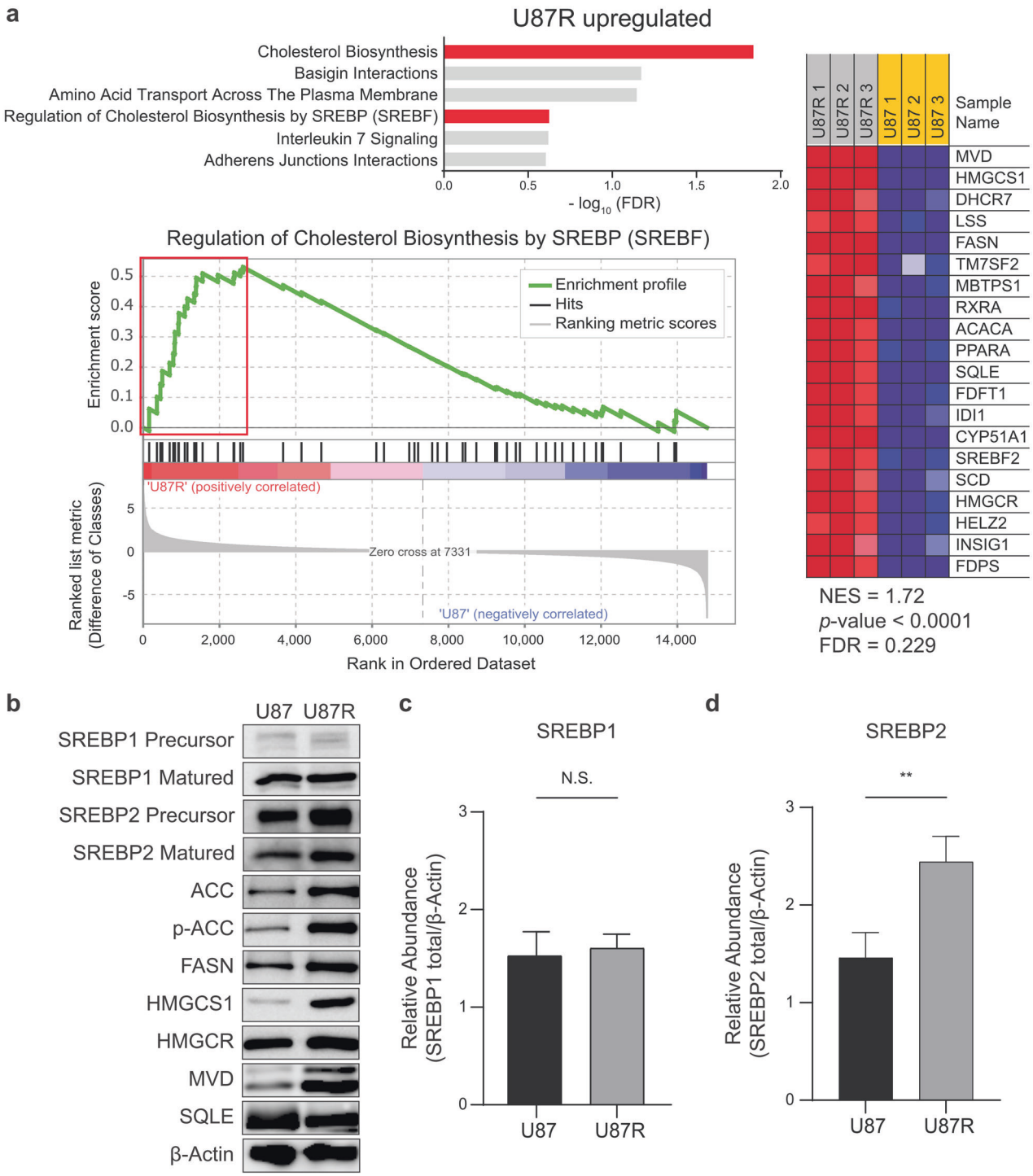

Fig. 3 Microarray and protein analysis on lipid-related pathways in glioblastoma cell lines. a Enrichment of the lipid synthesis pathway and its leading-edge genes. Top 6 upregulated pathways in U87R according to the FDR values by GSEA analysis on gene expressions related to lipid synthesis in U87 and U87R cells (upper). Enrichment plot from GSEA analysis for the "Regulation of Cholesterol Biosynthesis by SREBP" pathway from the microarray data (left). GSEA-derived heat maps of leading-edge genes in the red box on the left (right). **b** Protein level of lipid-related pathway in U87 and U87R cells. Beta-actin (β-Actin) was used as a loading control. Relative quantitation of SREBP1 (**c**) and SREBP2 (**d**) levels normalized to β-Actin from **b** ($n = 3$). Statistics are as in Fig. 2.

DISCUSSION

Here, we present a ternary relationship among cell shape, drug resistance, and lipid metabolism in relation to TMZ resistance in GBM cells. For the shape-resistance relationship, our data showed that acquisition of drug resistance is accompanied by changes in cell shapes in brain and lung cancer cells. Actually, there have been related reports in other types of cancer. When endometrial cancer became resistant to cisplatin, the cell height increased while the area decreased [21]. In addition, in breast cancer cells, when the cell shape (nuclear/cytoplasmic area ratio) was adjusted using artificially stiff substrates (PLLA and collagen coating), the nuclear/cytoplasmic area ratio decreased with the increase in the

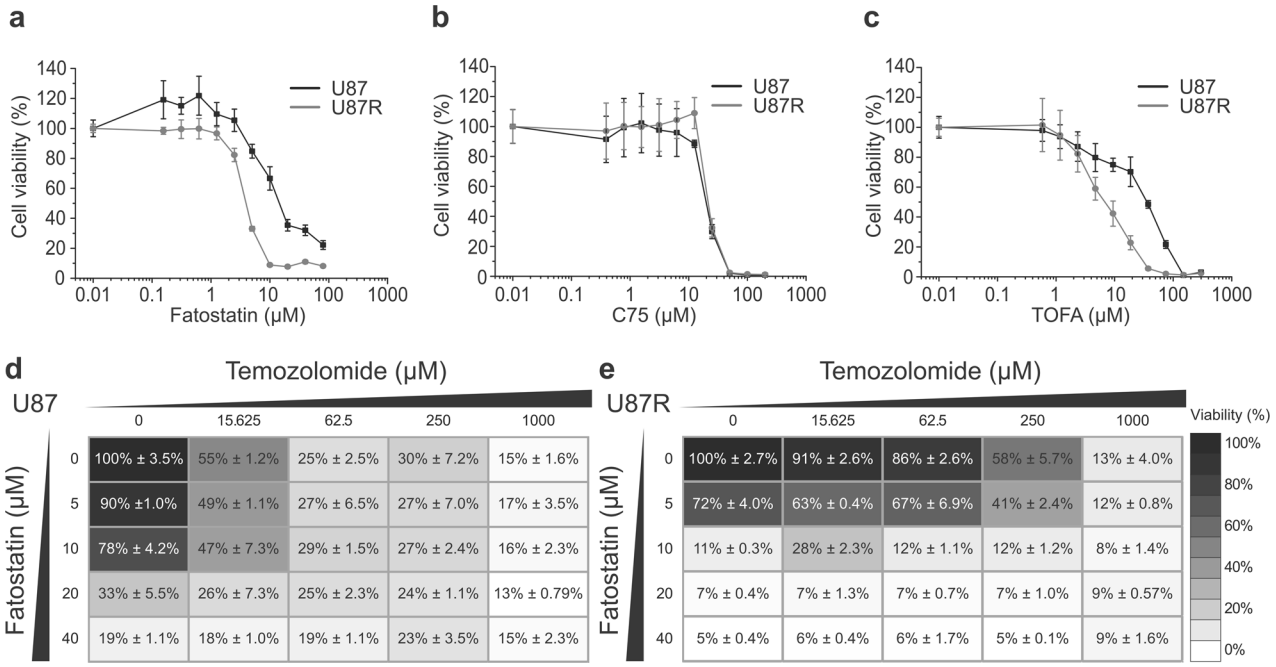

Fig. 4 Sensitivity of glioblastoma cell lines to drugs that inhibit lipid synthesis. Dose-response curves of U87 (black) and U87R (gray) cells after 5-day incubation with fatostatin (**a**), C75 (**b**), and TOFA (**c**), as determined with CCK-based cell viability assay. Error bars represent standard deviations ($n = 4$). Heatmaps of the raw dose-response landscape upon the combination treatment with TMZ and fatostatin on U87 (**d**) and U87R (**e**) cells. The numbers represent percent viability with standard deviations.

Table 1. IC_{50} values of inhibitors for lipid synthesis on U87 and U87R cells.

Cell lines	Drug		
	TOFA (μM)	C75 (μM)	Fatostatin (μM)
U87	39.98	21.04	8.69
U87R	7.51	21.69	3.93

IC_{50} values for cisplatin, vorinostat, and erlotinib [34]. Therefore, this study also provided possibly causal roles of cell shape changes in drug resistance. Very recently, an interesting study suggested that the drug resistance to ErbB family drugs and the associated mechanism can be predicted by machine-learning analysis of cancer cell morphology [35]. Therefore, our results and other studies indicate that cell shape-drug resistance relationship may be a frequent phenomenon across many types of cancer at least in vitro. Still, at this point, it is hard to generalize which particular shape characteristics confer drug resistance, and further studies may be needed. In addition, future in vivo studies may reveal if the shape-resistance relationship can be applied to histological examinations to determine the presence of drug-resistant subpopulation of cancer cells in tumor tissues.

It should not be surprising that cell shape is related to cellular lipid composition that can affect cell membrane. In addition to our results, previous studies provided some examples. T-47D human breast cancer cells, with typical flat, polygonal and cobblestone shape, first became spindle-shaped and then round and refractile upon prolactin or hydrocortisone treatment. These shape changes were concomitant with the increase in ORO stainable lipid droplets [24]. The relationship was also observed in a non-cancer context where erythrocytes exhibited higher morphological index and featured high cholesterol/phospholipid ratio, when exposed to high bilirubin level [25]. Lipids have also been implicated in cancer drug resistance. Triple-negative breast cancer (MDA-MB-436) cells exhibited increase in lipid droplets when they acquired doxorubicin resistance which was also accompanied by shape alterations to neuron-like shapes [23]. There have been several possible mechanisms on how lipids can affect drug resistance. Based on model membrane, a study showed that paclitaxel uptake decreased with lower FA unsaturation and higher cholesterol level, which could lead to decreased membrane fluidity, ultimately reducing drug uptake by passive diffusion or endocytosis [33, 36]. Another study showed that decrease in unsaturated FA caused less lipid peroxidation upon reactive oxygen species generation by anticancer drugs [37, 38]. As lipid peroxidation can trigger apoptosis and ferroptosis, lower unsaturation may confer drug resistance particularly to those drugs causing oxidative stress. Yet another study suggested that lipid droplets might act as a sink for hydrophobic drugs, leading to lower efficacy [39]. Related to this is electrostatic interaction as a factor for lipid-related drug uptake. For example, cisplatin, with its positive charge, interacted with negatively charged phospholipids, which led to reduced drug uptake [40]. For our case with TMZ in GBM cells, the first and second mechanisms seem applicable, considering the lower membrane fluidity and higher expression of a peroxide-removing enzyme in TMZ-resistant cells [12]. That is, the resistant cells seem to enhance lipid synthesis to increase the cholesterol content in the plasma membrane and decrease the unsaturated lipid ratio. The results should be lower membrane fluidity decreasing drug uptake and lower membrane peroxidation decreasing the efficacy of ROS-generating drugs. Overall, how lipids contribute to the drug resistance may not be uniformly explained and may need to be considered according to individual drugs and cancer types. As there is growing interest on physical properties affecting cellular phenotypes, such as phase separation or pressure [41–43], more effects of cell shape on physiology are expected to be revealed.

Another notable aspect of our study is the finding of SREBP2 as an important factor in TMZ resistance. Related to that, we showed that fatostatin, an inhibitor of SREBP could inhibit the TMZ-resistant cells as strongly as TMZ inhibited the sensitive cells.

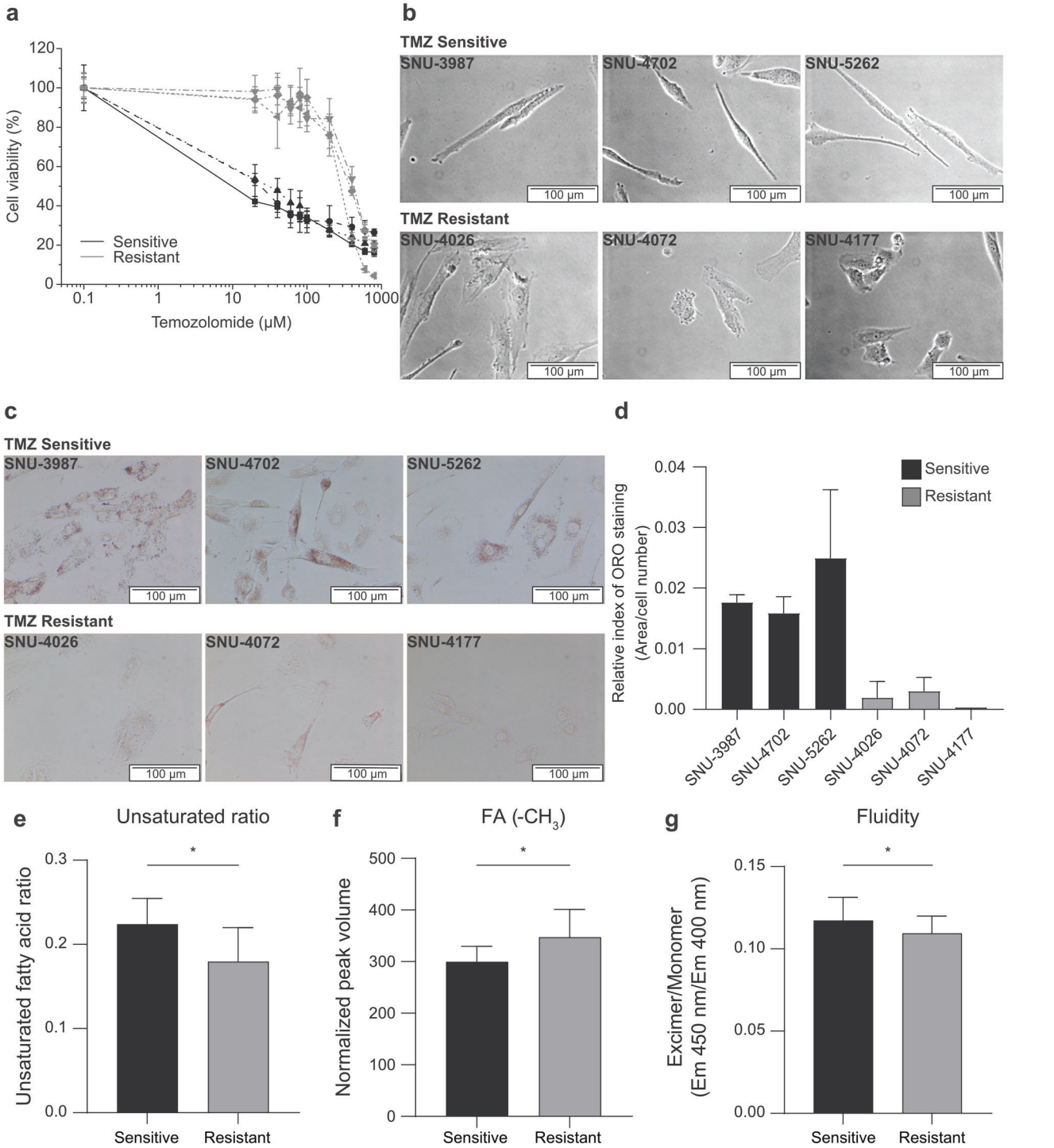

Fig. 5 TMZ sensitivity-lipid-cell shape relationship in patient-derived primary glioblastoma cells. a Dose-response curves of TMZ-sensitive (black) and TMZ-resistant primary cells (gray) cells after 5-day incubation with TMZ, as determined with CCK-based cell viability assay. **b** Cell shapes of TMZ-sensitive (upper) and TMZ-resistant primary cells (lower) were acquired by light microscopy. **c** ORO staining of TMZ-sensitive (upper) and TMZ-resistant primary cells (lower). Images were acquired by light microscopy. **d** Quantitation of ORO staining in **c** with ImageJ software. The staining levels were normalized against cell numbers ($n = 3$). **e** FA unsaturation ratio for patient-derived primary cells, obtained as in Fig. 2g. **f** Total FA levels determined by the mean peak volumes normalized by the total peak volumes from the HSQC spectra. **g** Membrane fluidity of primary glioblastoma cells measured by the ratio of the fluorescence of pyrene excimer ($E_x/E_m = 360/450$ nm) to monomer ($E_x/E_m = 360/400$ nm) ($n = 9$). Statistics are as in Fig. 2.

Although SREBP1 and SREBP2 have been conventionally implicated in FA and cholesterol synthesis [44], respectively, recent studies revealed that SREBP2 regulates SREBP1 and thus is a master regulator of general lipid synthesis [45, 46]. With our data showing SREBP2's higher expression in TMZ-resistant cells and fatostatin's effectiveness in these cells, SREBP2-driven lipogenesis may be a new vulnerability of GBM that can be therapeutically targeted. Currently, the only approved drug that targets GBM cells

Table 2. IC_{50} values of inhibitors for lipid synthesis on patient-derived primary cells.

Cell lines	Drug		
	TOFA (μM)	C75 (μM)	Fatostatin (μM)
SNU-3987	76.82	26.41	7.15
SNU-4702	46.43	27.8	7.9
SNU-5262	71.94	42.01	7.61
SNU-4026	54.61	29.84	13.37
SNU-4072	10.24	26.47	9.3
SNU-4177	19.81	32.08	11.8

is TMZ, and MGMT promoter methylation status has been used as a biomarker for TMZ resistance. However, a meta-analysis suggested that MGMT methylation status could change during tumor treatment, progression, or recurrence [47]. Therefore, another marker for TMZ resistance has been needed, and SREBP2 expression may be a possible candidate. Fatostatin inhibits the activation step of both SREBP1 and 2 [48], and its antitumor activity has been studied for several cancer types such as prostate, endometrial and breast cancers both in vitro and in vivo [49–51]. Still, it has not been evaluated for GBM in relation to TMZ-resistance. As SREBP1 has been shown to be involved in the growth of general GBM cells, and SREBP2 is important in TMZ resistance, fatostatin's dual inhibition of SREBP1 and 2 should be advantageous for inhibiting GBM growth. In addition, our data showed that there was not much difference in efficacy of fatostatin between TMZ-sensitive and resistant cells. Therefore, fatostatin could be used regardless of MGMT or TMZ-resistant status, possibly making it a more convenient option than TMZ.

In conclusion, our study revealed a ternary relationship among cell shape, lipids, and drug resistance where lipid synthesis is associated with cell shape changes and TMZ resistance. As fatostatin can inhibit SREBP that is upregulated in TMZ-resistance cells and inhibits U87/U87R cell growth regardless of TMZ-resistance, SREBP may serve as a new vulnerability for malignant GBM cancer.

ACKNOWLEDGEMENTS

This research was supported by Basic Science Research Program through the National Research Foundation of Korea (NRF) funded by the Ministry of Education (NRF-2020R1A6A3A01099440 to YJA).

AUTHOR CONTRIBUTIONS

MC, VHM, and DHK performed data acquisition, formal analysis, and investigation; HSK performed informatic analysis; JLK, SKL, and CKP established cell lines and helped conceptualization; YJA and SP conceptualized the project and wrote the manuscript.

ADDITIONAL INFORMATION

Supplementary information The online version contains supplementary material available at https://doi.org/10.1038/s41401-022-00984-6.

Competing interests: The authors declare no competing interests.

REFERENCES

1. Thakkar JP, Dolecek TA, Horbinski C, Ostrom QT, Lightner DD, Barnholtz-Sloan JS, et al. Epidemiologic and molecular prognostic review of glioblastoma. Cancer Epidemiol Biomark Prev. 2014;23:1985–96.
2. Allen BG, Bodeker KL, Smith MC, Monga V, Sandhu S, Hohl R, et al. First-in-human phase I clinical trial of pharmacologic ascorbate combined with radiation and temozolomide for newly diagnosed glioblastoma. Clin Cancer Res. 2019;25:6590–7.
3. Chen B, Chen C, Zhang Y, Xu J. Recent incidence trend of elderly patients with glioblastoma in the United States, 2000–2017. BMC Cancer. 2021;21:54.
4. Oike T, Suzuki Y, Sugawara KI, Shirai K, Noda SE, Tamaki T, et al. Radiotherapy plus concomitant adjuvant temozolomide for glioblastoma: Japanese mono-institutional results. PLoS One. 2013;8:e78943.
5. Al-Husseini MJ, Saad AM, El-Shewy KM, Nissan NE, Gad MM, Alzuabi MA, et al. Prior malignancy impact on survival outcomes of glioblastoma multiforme; population-based study. Int J Neurosci. 2019;129:447–54.
6. Starnoni D, Berthiller J, Idriceanu TM, Meyronet D, D'Hombres A, Ducray F, et al. Returning to work after multimodal treatment in glioblastoma patients. Neurosurg Focus. 2018;44:E17.
7. Zhang J, Stevens MF, Bradshaw TD. Temozolomide: mechanisms of action, repair and resistance. Curr Mol Pharmacol. 2012;5:102–14.
8. Cong ZX, Zhou Y, Wang JW, Pan H, Zhang DD, Zhang L, et al. Temozolomide and irradiation combined treatment-induced Nrf2 activation increases chemoradiation sensitivity in human glioblastoma cells. J Neurooncol. 2014;116:41–8.
9. Paravati AJ, Heron DE, Landsittel D, Flickinger JC, Mintz A, Chen YF, et al. Radiotherapy and temozolomide for newly diagnosed glioblastoma and anaplastic astrocytoma: validation of radiation therapy oncology group-recursive partitioning analysis in the IMRT and temozolomide era. J Neurooncol. 2011;104:339–49.
10. Carter TC, Medina-Flores R, Lawler BE. Glioblastoma treatment with temozolomide and bevacizumab and overall survival in a rural tertiary healthcare practice. Biomed Res Int. 2018;2018:6204676.
11. Lee SY. Temozolomide resistance in glioblastoma multiforme. Genes Dis. 2016;3:198–210.
12. Jin X, Kang S, Tanaka S, Park S. Monitoring the glutathione redox reaction in living human cells by combining metabolic labeling with heteronuclear NMR. Angew Chem Int Ed Engl. 2016;128:8071–4.
13. Singh N, Miner A, Hennis L, Mittal S. Mechanisms of temozolomide resistance in glioblastoma—a comprehensive review. Cancer Drug Resist. 2021;4:17–43.
14. Wenk MR. The emerging field of lipidomics. Nat Rev Drug Discov. 2005;4:594–610.
15. Casares D, Escribá PV, Rosselló CA. Membrane lipid composition: effect on membrane and organelle structure, function and compartmentalization and therapeutic avenues. Int J Mol Sci. 2019;20:2167.
16. Srivastava NK, Pradhan S, Gowda GAN, Kumar R. In vitro, high-resolution 1H and 31P NMR based analysis of the lipid components in the tissue, serum, and CSF of the patients with primary brain tumors: one possible diagnostic view. NMR Biomed. 2010;23:113–22.
17. Gopal K, Grossi E, Paoletti P, Usardi M. Lipid composition of human intracranial tumors: a biochemical study. Acta Neurochir. 1963;11:333–47.
18. Tugnoli V, Tosi MR, Tinti A, Trinchero A, Bottura G, Fini G. Characterization of lipids from human brain tissues by multinuclear magnetic resonance spectroscopy. Biopolymers. 2001;62:297–306.
19. Peetla C, Vijayaraghavalu S, Labhasetwar V. Biophysics of cell membrane lipids in cancer drug resistance: implications for drug transport and drug delivery with nanoparticles. Adv Drug Deliv Rev. 2013;65:1686–98.
20. Pallarés-Trujillo J, Domènech C, Grau-Oliete MR, Rivera-Fillat MP. Role of cell cholesterol in modulating vincristine uptake and resistance. Int J Cancer. 1993;55:667–71.
21. Yao T, Cao R, Xiao W, Pan F, Li X. An optical study of drug resistance detection in endometrial cancer cells by dynamic and quantitative phase imaging. J Biophotonics. 2019;12:e201800443.
22. Abuhammad S, Zihlif M. Gene expression alterations in doxorubicin resistant MCF7 breast cancer cell line. Genomics. 2013;101:213–20.
23. Sirois I, Aguilar-Mahecha A, Lafleur J, Fowler E, Vu V, Scriver M, et al. A unique morphological phenotype in chemoresistant triple-negative breast cancer reveals metabolic reprogramming and PLIN4 expression as a molecular vulnerability. Mol Cancer Res. 2019;17:2492–507.
24. Shiu RP, Paterson JA. Alteration of cell shape, adhesion, and lipid accumulation in human breast cancer cells (T-47D) by human prolactin and growth hormone. Cancer Res. 1984;44:1178–86.
25. Brito MA, Silva RM, Matos DC, da Silva AT, Brites DT. Alterations of erythrocyte morphology and lipid composition by hyperbilirubinemia. Clin Chim Acta. 1996;249:149–65.
26. Xu WJ, Wen H, Kim HS, Ko YJ, Dong SM, Park IS, et al. Observation of acetyl phosphate formation in mammalian mitochondria using real-time in-organelle NMR metabolomics. Proc Natl Acad Sci USA. 2018;115:4152–7.
27. Kohsaka S, Wang L, Yachi K, Mahabir R, Narita T, Itoh T, et al. STAT3 inhibition overcomes temozolomide resistance in glioblastoma by downregulating MGMT expression. Mol Cancer Ther. 2012;11:1289–99.

28. Chou TC. Drug combination studies and their synergy quantification using the Chou-Talalay method. Cancer Res. 2010;70:440–6.
29. Smith RL, Soeters MR, Wüst RCI, Houtkooper RH. Metabolic flexibility as an adaptation to energy resources and requirements in health and disease. Endocr Rev. 2018;39:489–517.
30. Silberman S, McGarvey TW, Comrie E, Persky B. The influence of ethanol on cell membrane fluidity, migration, and invasion of murine melanoma cells. Exp Cell Res. 1990;189:64–8.
31. Angelucci C, Maulucci G, Lama G, Proietti G, Colabianchi A, Papi M, et al. Epithelial-stromal interactions in human breast cancer: effects on adhesion, plasma membrane fluidity and migration speed and directness. PLoS ONE. 2012;7:e50804.
32. Edmond V, Dufour F, Poiroux G, Shoji K, Malleter M, Fouqué A, et al. Down-regulation of ceramide synthase-6 during epithelial-to-mesenchymal transition reduces plasma membrane fluidity and cancer cell motility. Oncogene. 2015;34:996–1005.
33. Hoy AJ, Nagarajan SR, Butler LM. Tumour fatty acid metabolism in the context of therapy resistance and obesity. Nat Rev Cancer. 2021;21:753–66.
34. Domura R, Sasaki R, Ishikawa Y, Okamoto M. Cellular morphology-mediated proliferation and drug sensitivity of breast cancer cells. J Funct Biomater. 2017;8:18.
35. Longden J, Robin X, Engel M, Ferkinghoff-Borg J, Kjær I, Horak ID, et al. Deep neural networks identify signaling mechanisms of ErbB-family drug resistance from a continuous cell morphology space. Cell Rep. 2021;34:108657.
36. Zhao L, Feng SS. Effects of lipid chain unsaturation and headgroup type on molecular interactions between paclitaxel and phospholipid within model bio-membrane. J Colloid Interface Sci. 2005;285:326–35.
37. Rysman E, Brusselmans K, Scheys K, Timmermans L, Derua R, Munck S, et al. De novo lipogenesis protects cancer cells from free radicals and chemotherapeutics by promoting membrane lipid saturation. Cancer Res. 2010;70:8117–26.
38. Yang WH, Huang Z, Wu J, Ding CKC, Murphy SK, Chi JT. A TAZ–ANGPTL4–NOX2 axis regulates ferroptotic cell death and chemoresistance in epithelial ovarian cancer. Mol Cancer Res. 2020;18:79–90.
39. Dubey R, Stivala CE, Nguyen HQ, Goo YH, Paul A, Carette JE, et al. Lipid droplets can promote drug accumulation and activation. Nat Chem Biol. 2020;16:206–13.
40. Speelmans G, Sips WHHM, Grisel RJH, Staffhorst RWHM, Fichtinger-Schepman AMJ, Reedijk J, et al. The interaction of the anti-cancer drug cisplatin with phospholipids is specific for negatively charged phospholipids and takes place at low chloride ion concentration. Biochim Biophys Acta. 1996;1283:60–6.
41. Boeynaems S, Alberti S, Fawzi NL, Mittag T, Polymenidou M, Rousseau F, et al. Protein phase separation: a new phase in cell biology. Trends Cell Biol. 2018;28:420–35.
42. Murthy SE, Dubin AE, Patapoutian A. Piezos thrive under pressure: mechanically activated ion channels in health and disease. Nat Rev Mol Cell Biol. 2017;18:771–83.
43. Elbaum-Garfinkle S. Matter over mind: liquid phase separation and neurodegeneration. J Biol Chem. 2019;294:7160–8.
44. Lee W, Seo YK. SREBP as a global regulator for lipid metabolism. J Life Sci. 2018;28:1233–43.
45. Vergnes L, Chin RG, De Aguiar Vallim T, Fong LG, Osborne TF, Young SG, et al. SREBP-2-deficient and hypomorphic mice reveal roles for SREBP-2 in embryonic development and SREBP-1c expression. J Lipid Res. 2016;57:410–21.
46. Rong S, Cortés VA, Rashid S, Anderson NN, McDonald JG, Liang G, et al. Expression of SREBP-1c requires SREBP-2-mediated generation of a sterol ligand for LXR in livers of mice. eLife. 2017;6:e25015.
47. Feldheim J, Kessler AF, Monoranu CM, Ernestus RI, Löhr M, Hagemann C. Changes of O6-methylguanine DNA methyltransferase (MGMT) promoter methylation in glioblastoma relapse-a meta-analysis type literature review. Cancers. 2019;11:1837.
48. Gholkar AA, Cheung K, Williams KJ, Lo YC, Hamideh SA, Nnebe C, et al. Fatostatin inhibits cancer cell proliferation by affecting mitotic microtubule spindle assembly and cell division. J Biol Chem. 2016;291:17001–8.
49. Fu Y, Zou T, Shen X, Nelson PJ, Li J, Wu C, et al. Lipid metabolism in cancer progression and therapeutic strategies. MedComm. 2020;2:27–59.
50. Gao S, Shi Z, Li X, Li W, Wang Y, Liu Z, et al. Fatostatin suppresses growth and enhances apoptosis by blocking SREBP-regulated metabolic pathways in endometrial carcinoma. Oncol Rep. 2018;39:1919–29.
51. Liu Y, Zhang N, Zhang H, Wang L, Duan Y, Wang X, et al. Fatostatin in combination with tamoxifen induces synergistic inhibition in ER-positive breast cancer. Drug Des Devel Ther. 2020;14:3535–45.